scientific data

Check for updates

OPEN

DATA DESCRIPTOR

BOston Neonatal Brain Injury Data for Hypoxic Ischemic Encephalopathy (BONBID-HIE): I. MRI and Lesion Labeling

Rina Bao[1,2] ✉, Ya'nan Song[1], Sara V. Bates[2,3], Rebecca J. Weiss[1], Anna N. Foster[1], Camilo Jaimes[2,3], Susan Sotardi[1], Yue Zhang[1], Randy L. Hirschtick[2,3,4], P. Ellen Grant[1,2,4] & Yangming Ou[1,2,4] ✉

Hypoxic ischemic encephalopathy (HIE) is a brain injury that occurs in 1 ~ 5/1000 term neonates. Accurate identification and segmentation of HIE-related lesions in neonatal brain magnetic resonance images (MRIs) is the first step toward identifying high-risk patients, understanding neurological symptoms, evaluating treatment effects, and predicting outcomes. We release the first public dataset containing neonatal brain diffusion MRI and expert annotation of lesions from 133 patients diagnosed with HIE. HIE-related lesions in brain MRI are often diffuse (i.e., multi-focal), and small (over half the patients in our data having lesions occupying <1% of the brain volume (including ventricles)). Segmentation for HIE MRI data is remarkably different from, and arguably more challenging than, other segmentation tasks such as brain tumors with focal and relatively large lesions. We hope that this dataset can help fuel the development of MRI lesion segmentation methods for HIE and small diffuse lesions in general.

Background & Summary

Accurate identification of brain injuries in neonatal brain magnetic resonance images (MRI)[1–3] is crucial to improve clinical care of neonates with hypoxic-ischemic encephalopathy (HIE), a brain disease that occurs in around 1 ~ 5/1000 term-born infants around birth[4,5]. HIE affects around 750,000 term-born neonates every year worldwide[4,5], costing about $2 billion/year in the US alone, let alone family burdens. Therapeutic hypothermia, the current clinical treatment of HIE, can reduce mortality and morbidity in high-income countries. Nevertheless, around 1/3 of patients still die or develop neurocognitive deficits by 2 years of age. MRI is used in over 50% of the >100 ongoing HIE-related clinical trials worldwide[6], for evaluating treatment effects[7–9], and helping discover clinical[10–12], biochemical[10,13–15], and serum[16–18] biomarkers. Accurate identification of brain lesions in neonatal brain MRIs[1–3] is needed for disease prognosis, a better understanding of the neural basis of disease progression, and more timely evaluations of novel therapeutic effects.

HIE lesions are often diffuse (i.e., multi-focal), and small; hence, algorithms that have shown great promise in segmenting big and focal lesions, such as brain tumors and acute strokes, often encounter challenges when directly applied to MRIs of HIE patients. Indeed, many (over half) patients had lesions occupying <1% of brain volume, as shown in Fig. 1. As a result, the segmentation accuracy measured by the Dice overlap with U-Net[19] and other state-of-the-art machine/deep learning algorithms on HIE remains at around 0.5[20], whereas Dice is over 0.8 when segmenting brain tumors[21,22].

A major hurdle in developing algorithms for small diffuse lesions, such as HIE lesions, is the lack of public data. Public data with expert annotations of lesions have fueled the advancement of machine learning algorithms to segment brain tumors[23], stroke lesions[24], multiple sclerosis lesions[25,26], and numerous other diseases in the brain or other organs[27,28]. However, to date, there is no public MRI data with expert annotations available for HIE lesions.

[1]Boston Children's Hospital, Boston, MA, USA. [2]Harvard Medical School, Boston, MA, USA. [3]Massachusetts General Hospital, Boston, MA, USA. [4]These authors contributed equally: Randy L. Hirschtick, P. Ellen Grant, Yangming Ou. ✉e-mail: rina.bao@childrens.harvard.edu; yangming.ou@childrens.harvard.edu

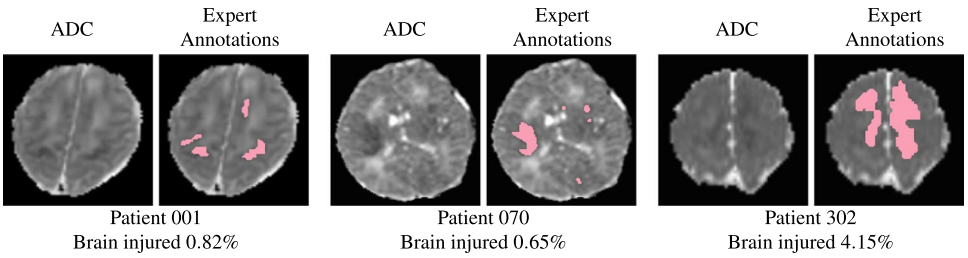

Fig. 1 Lesions associated to hypoxic ischemic encephalopathy (HIE) are typically diffuse (i.e., multi-focal) and small. Here we show two representative images for 3 HIE patients. For each patient, in the left panel: apparent diffusion coefficient (ADC) maps that are clinically used to identify HIE lesions; in the right panel: manually-annotated lesions (shown in pink) overlaid on the ADC map. We listed the percentage of the whole brain volume (including ventricles) being injured at the bottom (i.e., lesion volume divided by the whole brain volume).

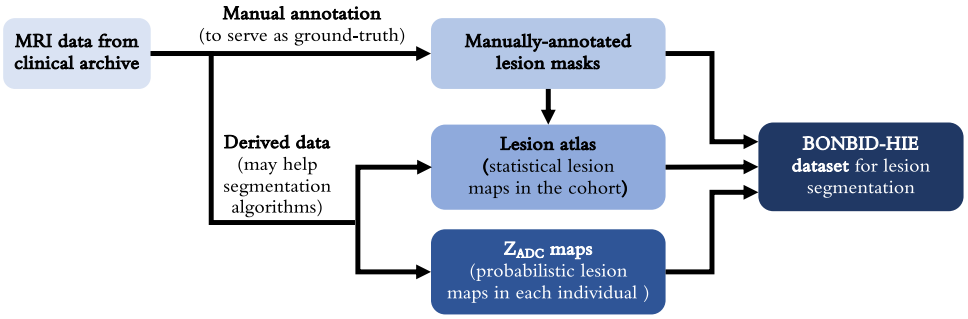

Fig. 2 A schematic diagram showing the steps performed on the BONBID-HIE data for release.

We present BOston Neonatal Brain Injury Dataset for Hypoxic Ischemic Encephalopathy (BONBID-HIE), an open-source, comprehensive, and representative MRI dataset for HIE. This paper introduces the first part of the BONBID-HIE data. This release contains raw and derived diffusion parameter maps, as well as manually-annotated lesion masks, for 133 HIE patients. Our data was from Massachusetts General Hospital. It includes MRIs from different scanners (Siemens 3T and GE 1.5T), different MRI protocols, and from patients of different races/ethnicities and ages (0-14 days postnatal age). Part I of our data release (this paper) focuses on lesion detection, while Part II (a follow-up paper) will focus on clinical, treatment, and neurologic outcome data for further developing prognostic biomarkers.

Our data contains voxel-wise annotation of HIE lesions beyond the brain region-level rough localization of abnormalities for two reasons. First, extractions of subsequent features, such as lesion volumes, lesion geometry, within-lesion signal heterogeneity, within-lesion histogram analysis, will require voxel-level identification of lesions. Such features are expected to offer additional information for predicting the neurological outcomes by 2 years of age, which is the ultimate goal for the design of prognosis biomarkers. Second, it is possible to derive brain-regional-level injuries from the voxel-wise lesion detection

Methods

Study Approval and Data Security. This work was approved by Institutional Review Boards (IRBs): IRB-P00025916 (PI: Y. Ou) at Boston Children's Hospital and IRB-2015P001651 (PI: Y. Ou) at Massachusetts General Hospital. Consent was waived because the retrospective nature of this work: many of the patients have already completed follow-up, live at a great distance from the hospitals, or the contact information is not up to date. Data were kept in encrypted folders on password-protected computers within the two hospitals' firewalls. Also, anonymization included removing identifiable information (medical record number, date of birth, name, physician's name, visit dates, etc.) in the clinical report and imaging header. Patient names were replaced by MGHNICU_001, MGHNICU_002,… Brain images have undergone defacing to remove the risk of 3D rendering that may recognize the facial features.

Overview. Figure 2 illustrates the overall data archiving process. MRI data for this dataset were acquired from MGH. Manual annotations were performed to create lesion masks for each individual patient, which served as the ground truth. These lesion masks were then aggregated to form a lesion atlas, representing statistical lesion maps across the cohort. Concurrently, the collected MRI data were processed to generate Z_{ADC} maps, which were probabilistic lesion maps for each individual. In the following sections, we will discuss each step involved in creating the BONBID-HIE dataset in detail.

Retrospective Data Collection. Data was retrospectively collected from MGH. Inclusion criteria were: (1) term-born; (2) clinical diagnosis of HIE; (3) initially treated at MGH between 2001 and 2018; (4) no comorbidities such as hydrocephalus or congenital syndromes; and (5) high-quality MRI acquired in Day 0-14 after birth

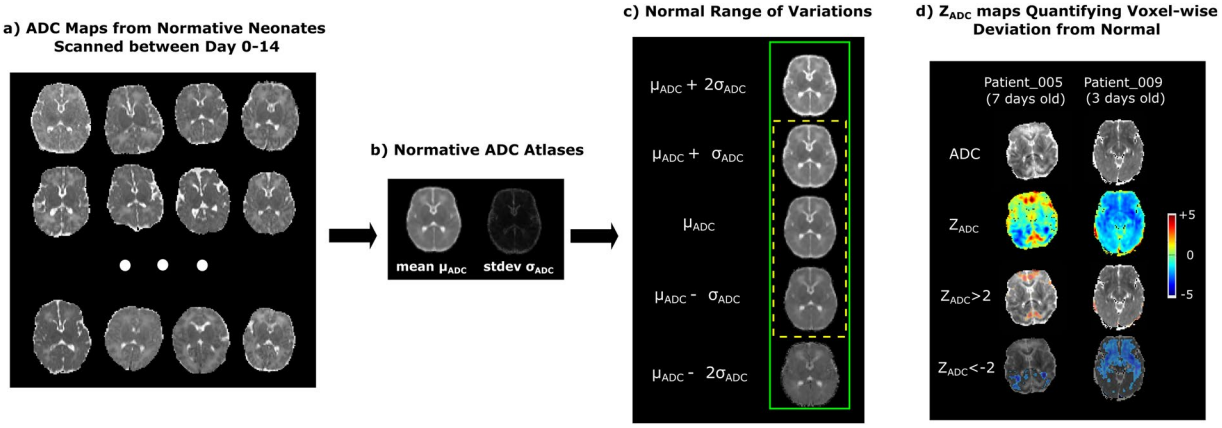

Fig. 3 The generation and concept of Z_{ADC} maps. (**a**) Examples of ADC maps from normative subjects, which were warped into the same space using unbiased group-wise DRAMMS registration to generate (**b**) the mean and standard deviation ADC atlases. (**c**) One (yellow dashed box) or two (green solid box) standard deviations above and below the mean ADC atlas define the normal ranges of voxel-wise ADC variations. (**d**) Our novel Z_{ADC} map quantifies voxel-wise deviations from the mean ADC map in (**b**). The cool/warm colors in (**d**) represent voxels with ADC values lower/higher than the mean ADC at the same anatomic location, according to the scale bar on the right.

(visually checked by RW, AF, YO). Exclusion criteria were: (1) excessive motion artifacts or missing images; or (2) primary perinatal stroke, focal artery ischemic stroke, or hemorrhage.

Clinical characteristics and demographic information were retrospectively gathered from the electronic health records (EHRs). The clinical variables included maternal information during pregnancy and delivery, as well as infant information. More detail can be found in the "Data Records" Section.

MRI data was downloaded from MGH Radiology Department clinical archives using the mi2b2 search engine[29]. MRIs were acquired on either a GE 1.5T Signa scanner (N=52, scanned during 2001-2012), or, a Siemens 3T TrioTim or PrismaFit scanner (N=81, scanned during 2012-2018). Diffusion tensor sequences on all scanners had the protocol as follows: Time of Repetition (TR) = 7500–9500 *ms*, Time of Echo (TE) = 80–115 *ms*, and b = 1000 s/mm^2. The GE 1.5T scanner had resolution 1.5 × 1.5 × (2.0–4.0) mm^3 and (6–60) diffusion directions, while the Siemens 3T scanner had a resolution 2 × 2 × 2 mm^3 and (25–60) diffusion directions. Apparent diffusion coefficient (ADC) maps were directly generated by the scanners (with the Advantage Windows Workstation for GE scanners[30,31] and with Syngo software for Siemens scanners[32]).

MRI Pre-processing. Besides the raw NIfTI image as converted from the DICOM files, we also generated several processed images. The pre-processing steps included: N4 bias correction[33], field of view normalization[34], multi-atlas skull stripping for the ADC maps[35], and deformable registration of each patient's ADC map to a normative 0-14 day neonatal brain ADC atlas[36], by the Deformable Registration via Attribute Matching and Mutual-Saliency weighting (DRAMMS) software[37], which has been extended-validated for lifespan ages in various MRI sequences[38]. This normative ADC atlas was constructed from ADC maps of 13 healthy individuals acquired 0-14 days after birth (Fig. 3a) with our extensively-validated MRI analysis pipeline[34,35,37,38]. All software packages used in this pre-processing pipeline are publicly available and have been validated in processing both research and clinical MRI scans across ages[39–43].

Multi-Expert Consensus Annotation of Lesions As Ground-Truth. HIE lesions had been qualitatively described in radiology reports that were part of the clinical flow. In this clinical process, ADC maps were used as the primary images, in addition to structural MRIs, to identify HIE abnormalities[44–46]. To convert the description of lesions in the radiology report into voxel-by-voxel expert annotation, we used a two-step expert consensus approach. First, HIE lesions were manually annotated as a binary mask on the ADC maps in the patient's raw image space, using the MRICroN software, according to the neuroradiology reports. This was done primarily by a clinical fellow (YS; >3 years of experience in general medicine and >1.5 years of neuroradiology training by practicing neuroradiologists at BCH specifically for HIE-related neuroimaging interpretation). The annotation protocol asked the primary annotator to label voxels as the expert deemed abnormal by his/her expertise, only in those brain regions mentioned in the clinical radiology report, and to leave uncertainties or disagreements for the subsequent expert consensus process. The annotations started from the axial slice and were subsequently modified in the coronal and sagittal planes for the 3D integrity of lesion regions. Second, in those 27 patients where uncertainties or disagreement between the primary annotator (YS) and the clinical radiology report occurred, we created a consensus lesion mask based on discussions among three more experienced pediatric neuroradiologists (CJ, SS, and PEG; >5, >5, and >20 years of experience practicing clinical pediatric neuroradiology), in a simple majority manner. This single set of lesion annotations on the ADC maps, the first for HIE, reflects the collective decision among the neuroradiologists who read the images at the time of clinical care, the primary annotator (YS), and 3 more experienced pediatric neuroradiologists (CJ, SS, PEG). This multi-expert consensus annotation process is less biased than a single-expert annotation. Our ongoing work on a 21-site HIE dataset is using more resource- and expertise-demanding multi-expert independent approach.

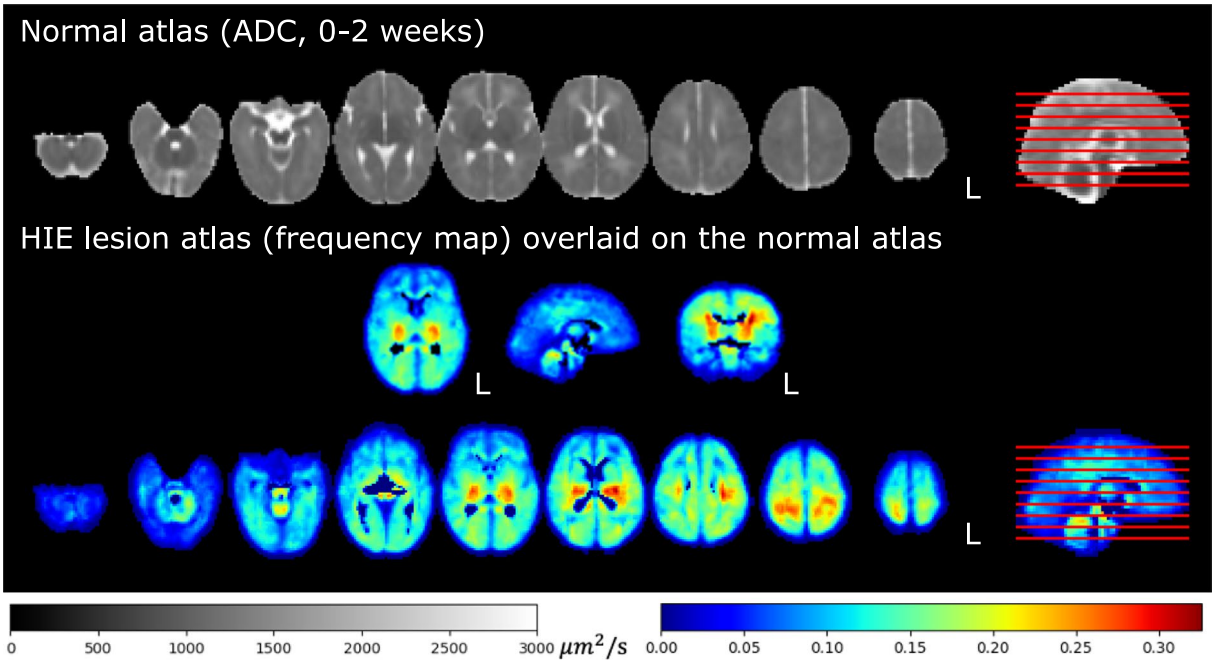

Fig. 4 Statistical lesion atlas quantifying the voxel-wise lesion frequency in our cohort of N = 133 patients in the normal 0-14 days ADC atlas space.

Generation of Z_{ADC} Maps for Each Patient– Derived to Aid Automated Lesion Segmentation. Neuroradiologists identify acute brain injury from HIE as regions with low ADC values. Low ADC values represent a reduced water diffusion, which occurs in the first week after birth due to ischemic necrosis resulting from the hypoxic ischemic insult[6]. However, a dilemma is, what ADC value is considered abnormally low versus just low within the normal variation? The normal variations of ADC values differ across brain regions[36,47], making this question difficult even for experienced neuroradiologists. For example, a voxel with an ADC value of 800 ($\times 10^{-6} mm^2/s$) may be considered normal at one brain region, whereas another voxel with an ADC value of 900 ($\times 10^{-6} mm^2/s$) may be considered lesioned at another brain region, if the normal ranges of ADC variations in the two brain regions are 700–900 and 950–1100 (same unit), respectively.

To address this dilemma, we have developed Z_{ADC} maps to normalize and make ADC values comparable across brain voxel locations[39]. First, a normative ADC atlas was generated from scans of 13 normative neonates (Fig. 3a). This atlas quantifies the mean ADC values and standard deviation at every voxel[36] (Fig. 3b), and hence the normal range of variations at each voxel (Fig. 3c). Then, we converted each patient's ADC map (first row, Fig. 3d) into a Z_{ADC} map (second row, Fig. 3d). The Z_{ADC} maps compared the patient's ADC value at each voxel to the normal variations at the corresponding voxel in the atlas. In a nutshell, Z_{ADC} maps quantify how many standard deviations away a patient's ADC value at a voxel is from the normal mean at the same anatomical location.

Specifically, a deformation (D) was computed, which mapped every voxel x in the patient's ADC map to its anatomically-corresponding location $D(x)$ in the atlas space. The normal range of ADC variation per voxel was defined by the mean $\mu(D(x))$ and standard deviation $\sigma(D(x))$ denoted for that voxel across all healthy neonates. Finally, the patient's ADC value I_x at voxel x was converted to a Z value: $Z_x = (I_x - \mu(D(x)))/\sigma(D(x))$. We calculated the Z_{ADC} map, which resides in the patient's raw ADC image space, for each patient. This offers an option for developing anatomy-aware lesion segmentation algorithms[48].

It is important to note that Z_{ADC} maps were not part of the scanner-generated images, nor stored in scanner or PACS. Z_{ADC} maps were not used in expert consensus annotation of lesions, which serve as ground truth for computer-assisted lesion detection. Z_{ADC} maps were generated in post-processing steps, to aid the computer-assisted lesion detection. Results from Z_{ADC} maps were validated against expert consensus of lesion annotation for the accuracy of computer-assisted lesion detection algorithms. Algorithm developers have options to use or not use Z_{ADC} maps in their lesion segmentation algorithms.

Construction of Statistical Lesion Atlases for the Cohort. The same deformation field that was computed by the non-rigid registration from the patient's skull-stripped ADC map to the normal ADC atlas was used to transform the binary brain lesion maps of each patient into the normal neonatal ADC atlas space[37]. The transformed binary lesion masks were then summed and divided by the total number of patients at each voxel. This led to a statistical lesion atlas that quantifies voxel-wise frequency, or probability, of HIE lesions in our cohort, as illustrated in Fig. 4.

The normal neonatal ADC atlas is part of the release, to offer an option to algorithm developers. An algorithm for HIE lesion detection can opt to use the normal ADC atlas to contrast HIE-related abnormality, or choose not to use this atlas. We would clarify that the HIE cohort, on which the lesion detection algorithms are to be developed, only contains data from patients with clinically confirmed HIE diagnosis.

A. Demographics and Clinical Characteristics		
Maternal Information		
Maternal age at delivery (years)	29.5 ± 6.7	N=133
Race	White (43), Black or African American (7), Hispanic or Latino (15), Multi Race (5), Unknown (57), Other (6)	N=133
Delivery	C-section (78), Vaginal (55)	N=133
Antepartum hemorrhage	Yes (29), No (104)	N=133
Thyroid dysfunction	Yes (5), No (128)	N=133
Pre-eclampsia	Yes (9), No (124)	N=133
Fetal decels	Yes (72), No (61)	N=133
Shoulder dystocia	Yes (8), No (125)	N=133
Chorioamnionitis	Yes (20), No (108)	N=133
Emergency c-section	Yes (69), No (58)	N=133
Neonatal Information		
Age at scan (days)	3.9 ± 2.7	N=133
Gestational age at birth (weeks)	39.1 ± 1.9	N=133
Birth weight (g)	3321.9 ± 615.9	N=133
Infant head circumference (cm)	34.2 ± 1.4	N=85
Sex	Male (74), Female (59)	N=133
1-minute APGAR scores	1.9 ± 1.7	N=133
5-minute APGAR scores	4.2 ± 2.3	N=132
10-minute APGAR scores	5.3 ± 2.1	N=118
Lowest pH value in umbilical cord	7.00 ± 0.20	N=129
Therapeutic hypothermia before MRI?	Yes (86), No (47)	N=133
Endotracheal tube (ETT) in NICU	Yes (78), No (47)	N=125
Total parenteral nutrition (TPN) in NICU	Yes (111), No (21)	N=133
Seizures NICU	Yes (64), No (69)	N=133
Length of stay in NICU (days)	12.10 ± 9.92	N=133

B. Lesion Characteristics (N=133)	
Whole-brain lesion volume – minimum	0 mm3 (0% of the brain injured)
Whole-brain lesion volume - 25th percentile	441.96 mm3 (0.10% of the brain injured)
Whole-brain lesion volume - median	2765.63 mm3 (0.63% of the brain injured)
Whole-brain lesion volume - 75th percentile	24264.27 mm3 (4.86% of the brain injured)
Whole-brain lesion volume - maximum	412120.00 mm3 (82.59% of the brain injured)

C. Number of Patients by Percentage of Lesions in the Brain (N=133)	
[0%, 1%) of the brain being injured	55.64% (N=74)
[1, 5%) of the brain was injured	19.55% (N=26)
[5, 10%) of the brain was injured	5.26% (N=7)
[10, 20%) of the brain was injured	4.51% (N=6)
[20, 50%) of the brain was injured	8.27% (N=11)
[50, 100]% of the brain was injured	6.77% (N=9)

D. Scanner (N=133)	
GE 1.5T	39% (N=52)
Siemens 3T	61% (N=81)

Table 1. Cohort characteristics (N=133).

Data Records

The dataset is available on Zenodo (https://zenodo.org/records/10602767)[49]. All data has been made publicly available under the CC BY license (https://creativecommons.org/licenses/by/4.0/legalcode).

Dataset Characteristics. Table 1A lists the demographics and clinical characteristics of mothers and neonates. Maternal information includes demographics (age at delivery, race), birth mode (C-section or vaginal), and complications during pregnancy and delivery. Neonatal information includes demographics (age at MRI scan, gestational age at birth, birth weight, head circumference, sex), birth conditions (1/5/10-minute Apgar scores, lowest pH value in umbilical cord), treatment (hypothermia or not), and complications in the neonatal intensive care unit (NICU), including seizure (yes/no), the length of stay (in days), the use of endotracheal tube (ETT, yes/no), and the administration of total parenteral nutrition (TPN, yes/no). In each row, we also listed the number of patients who had such information available.

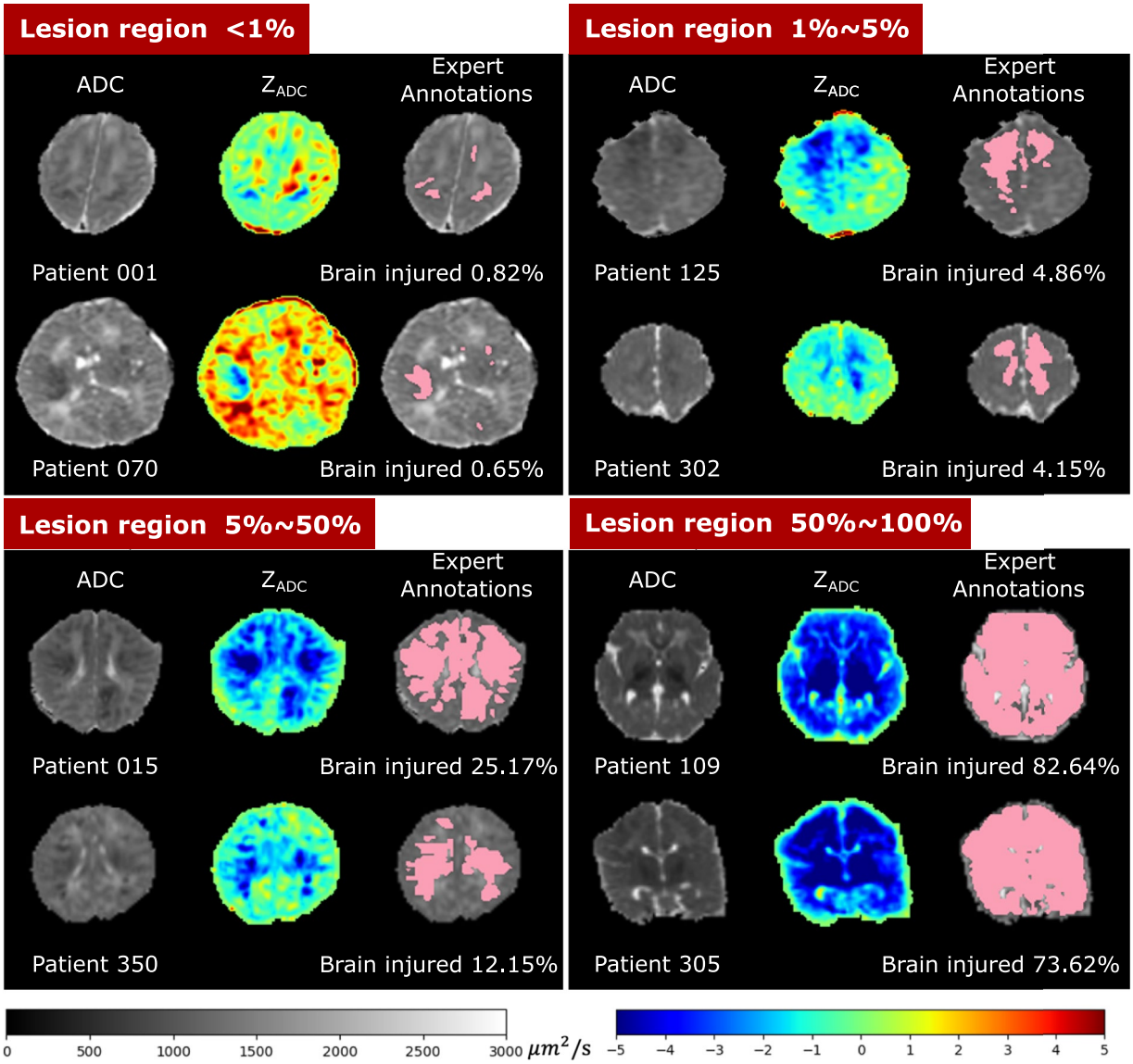

Fig. 5 Visualization of patients with different lesion percentages. In every patient, the left image is the ADC map (skull stripped) with range of ADC values designated by the gray scale bar, the middle is the computed Z_{ADC} map with range of Z-scores designated by the rainbow scale bar, and the right image is the expert-annotated lesion regions (pink) overlaid on the ADC map. Percentages of injury were calculated by the volume of the expert-annotated lesion regions divided by algorithm-extracted whole brain volumes (including ventricles).

Table 1B quantifies the distribution of the absolute lesion volumes (in mm^3) and relative lesion volume (percentage of the brain being injured). Here, the relative lesion volume was calculated by the volume of the expert-annotated lesion regions divided by the algorithm-extracted whole brain volumes (including ventricles) [34,35]. The median lesion volume accounted for 0.63% of the whole brain volume. This confirms that over half of the patients had less than 1% of the brain being injured. Table 1C further calculates the distribution of the relative lesion volumes (by the percentage of the brain volume being lesioned). The absolute and relative volumes were both computed in the patient's raw ADC image space. The minimum lesion was 0 mm^3, which is a common issue in HIE – mild HIE cases may not show explicit lesions in neonatal MRIs[50–52].

Figure 5 shows the ADC map, Z_{ADC} map, and expert annotations of example patients with different HIE lesion percentages. Two patients are shown in each of the four groups: those with lesions occupying $< 1\%$ (upper left panel), 1–5% (upper right panel), 5–50% (lower left panel), and 50–100% (lower right panel) of the whole brain volume. Overall, around 1 in 2 (55.64%) patients had HIE lesions occupying less than 1% of their brain volume, and 3 in 4 patients (75.19%) patients had lesions occupying less than 5% of their brain. This confirms that HIE lesions detectable in the diffusion MRI in our cohort are often small.

Data structure and file formats. All medical imaging files were exported from the Picture Archiving and Communication System (PACS) and converted into the NIfTI format. Segmentation masks created by expert

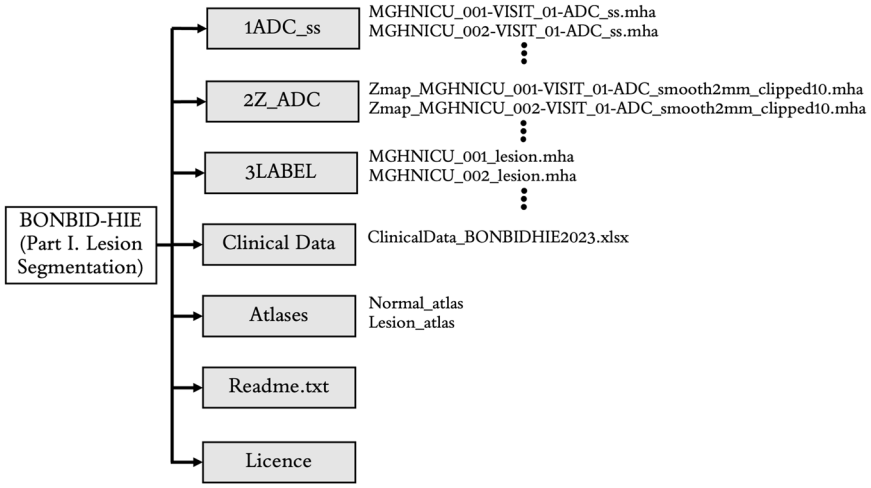

Fig. 6 Folder structure of the BONBID-HIE dataset (Part I. Lesion Segmentation).

annotations were also saved in NIfTI format. Corresponding scanner metadata from the Digital Imaging and Communications in Medicine (DICOM) header in the .json file format is provided with the released dataset. All data in the BONBID-HIE dataset was separated into a training dataset (N=89) and a test dataset (N=44). Both the training and testing contain data from both scanners (GE 1.5T Signa and Siemens 3T Trio). The split between the training and testing dataset has been performed (RB, YO) so that both sets include a similar variance of HIE lesion patterns as shown in Table 1C.

The data is organized in the format shown in Fig. 6. BONBID-HIE provides, per patient: (i) 1ADC_ss: skull stripped ADC map; (ii) 2Z_ADC: Z_{ADC} map; (iii) 3LABEL: expert lesion annotations; and (iv) clinical data: clinical variables as written in Table 1A. There is also (v) Atlases: a folder for the normal and lesion atlases; (vi) a readme.txt file: a text file to provide information on this data organization; and (vii) the license file of the BONBID-HIE dataset.

Technical Validation

Representativeness of patient cohort. Our data is representative of HIE cohorts in the developed countries. At least three characteristics of our data agree with documented clinical knowledge about HIE.

Lesion distribution in space agrees with clinical knowledge. Our statistical lesion atlas in Fig. 4 shows that HIE lesions can occur anywhere in the brain. The regions most frequently injured included the basal ganglia, internal capsules, thalamus, perirolandic cortex/subcortical white matter, temporal lobes, cerebral white matter, brainstem, and vermis (red, orange, and yellow regions in Fig. 4). This lesion atlas map coincides with clinical knowledge of brain regions often vulnerable to HIE injuries[2,6,13]. Indeed, HIE-related injuries in these regions have been key criteria in expert MRI scoring systems, which are used to assess the severity of HIE. Examples include the NICHD Neonatal Research Network (NRN)[2], the Barkovich[53], the Weeke-deVeries[3], and the Trivedi[54] scoring systems. In addition, lesions appeared in less than 35% of the patients at any given voxel, according to the color bar in this figure. This confirms the clinical knowledge that HIE lesions are diffuse, spatially distributed, and almost half to two-thirds of the HIE patients have no or minimal injuries on diffusion imaging, at least in patients in the USA[51,52].

Lesion distribution in time agrees with clinical knowledge. Figure 7(a) shows the percentage of the whole brain volume being lesioned at different postnatal ages. The lesion percentage in the ADC maps came down to almost 0 in the 9 patients who underwent MRI scans after postnatal day 7. This agrees with the clinical knowledge that HIE-related lesions are more detectable in ADC maps during 0-7 postnatal days or in T1/T2-weighted images than in relatively later scans (after postnatal day 7)[2,46,52].

ADC evolvement with age agrees with clinical knowledge. Figure 7(b) shows the whole-brain average ADC values of all patients (each dot is one patient). In normal cohorts, ADC values drop rapidly in the early postnatal life (see Figures 4 and 5 in[36], and Figures 3 and 4 in[47]). However, the presence of HIE-related abnormalities disrupted this trend – HIE patients undergoing earlier MRIs (0-7 postnatal days) had decreased ADC values in a larger precentage of the brain (Fig. 7(a)), so the ADC values in 0-7 postnatal days were at similar or even lower levels than ADC values in 7-14 postnatal days among HIE patients (Fig. 7(b)). This has also been documented in HIE literature[55,56].

Utility of ADC maps and Z_{ADC} maps in Automated Lesion Segmentation. The only ground truth for lesion segmentation in our released data is the expert consensus of lesion annotations. Our data release includes Z_{ADC} maps as an option to algorithm developers. To demonstrate the utility of the computed Z_{ADC}

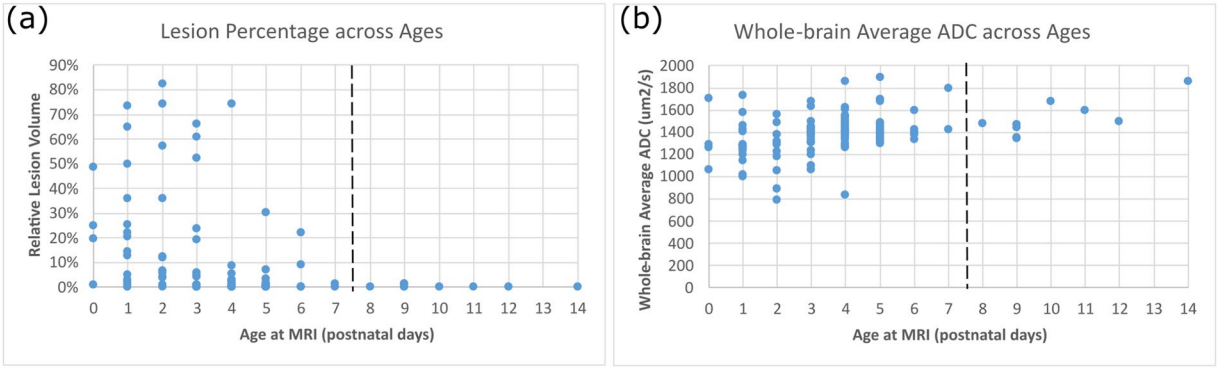

Fig. 7 Representativeness of our cohort for (**a**) lesion distribution across ages; and (**b**) whole-brain ADC values across ages. In both panels, each dot denotes a patient in our cohort.

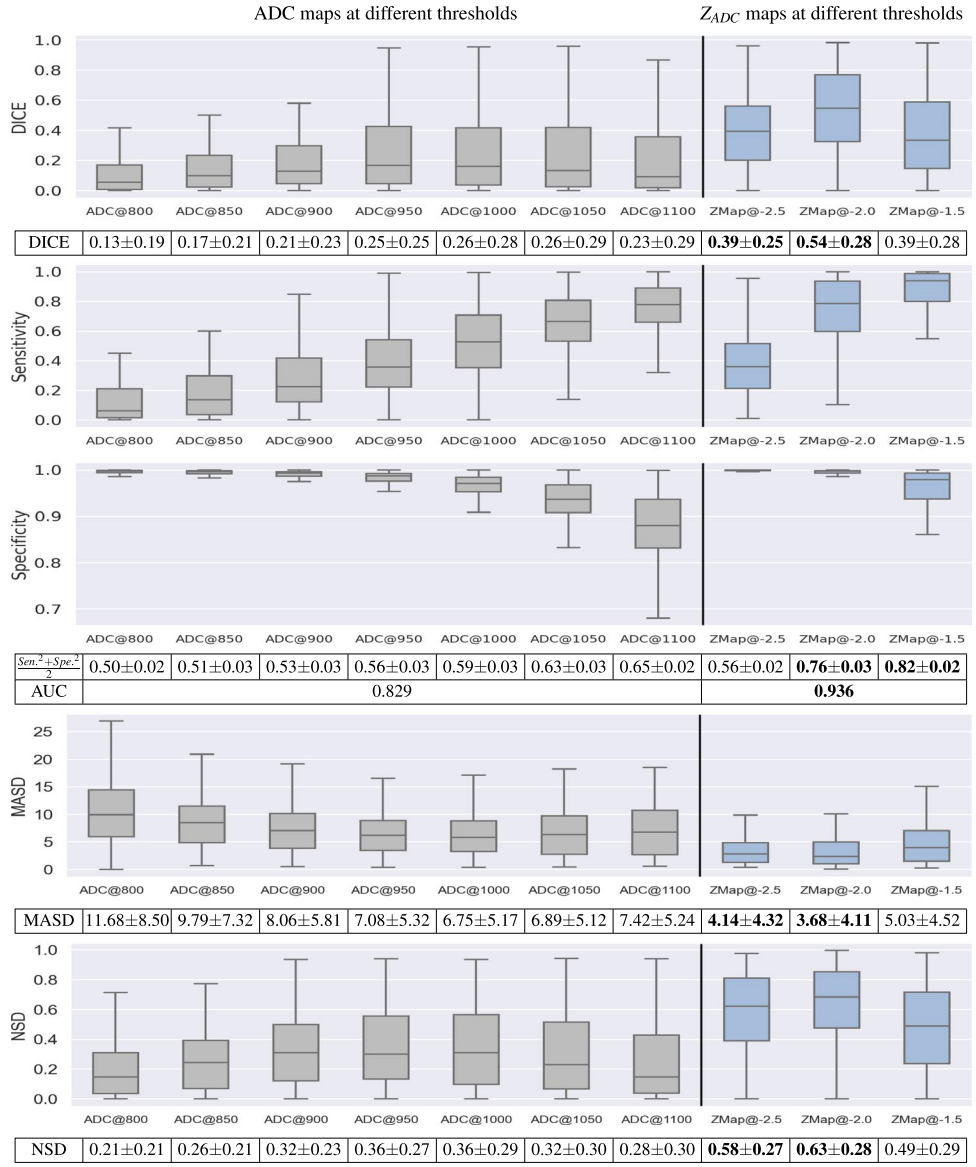

	ADC@800	ADC@850	ADC@900	ADC@950	ADC@1000	ADC@1050	ADC@1100	ZMap@-2.5	ZMap@-2.0	ZMap@-1.5
DICE	0.13±0.19	0.17±0.21	0.21±0.23	0.25±0.25	0.26±0.28	0.26±0.29	0.23±0.29	**0.39±0.25**	**0.54±0.28**	0.39±0.28
$\frac{Sen.^2+Spe.^2}{2}$	0.50±0.02	0.51±0.03	0.53±0.03	0.56±0.03	0.59±0.03	0.63±0.03	0.65±0.02	0.56±0.02	**0.76±0.03**	**0.82±0.02**
AUC	0.829								**0.936**	
MASD	11.68±8.50	9.79±7.32	8.06±5.81	7.08±5.32	6.75±5.17	6.89±5.12	7.42±5.24	**4.14±4.32**	**3.68±4.11**	5.03±4.52
NSD	0.21±0.21	0.26±0.21	0.32±0.23	0.36±0.27	0.36±0.29	0.32±0.30	0.28±0.30	**0.58±0.27**	**0.63±0.28**	0.49±0.29

Fig. 8 Accuracy of thresholding-based lesion segmentation on ADC and Z_{ADC} maps with different threshold values, measured by Dice, sensitivity, sepecificity, $\frac{Sen.^2+Spe.^2}{2}$, AUC, MASD and NSD. Bold texts in the tables beneath the figure panels highlight the two scenarios with the lowest MASD scores (lower is more accurate lesion detection), or the two scenarios with the highest Dice, AUC and NSD metrics (higher is more accurate lesion detection).

maps, we compared the accuracies of using ADC or Z_{ADC} maps for lesion segmentation. We attempted simple thresholding of ADC and Z_{ADC} maps, at several threshold values, for segmenting HIE lesions. Although simple, thresholding-based segmentation accuracy is a strong indicator for segmentation accuracies in more sophisticated machine/deep learning algorithms[57]. For ADC maps, we used different thresholds ranging from 800-1100 $\mu m^2/s$, as suggested in the literature[46,58–61]. For Z_{ADC} maps, we used thresholds -1.5, -2, and -2.5. Voxels in patient MRIs with ADC values 1.5 to 2.5 standard deviations below the average ADC values from healthy controls were considered abnormally low and hence, lesioned. The choice of thresholds around -2 in Z_{ADC} maps was also based on the hypothesis of a normal distribution of ADC values at each voxel across subjects[36,39].

We evaluated the accuracy of these maps compared to expert-annotated ground-truth masks using the Dice coefficient, sensitivity, specificity, Mean Average Surface Distance (MASD)[62,63], and Normalized Surface Distance (NSD)[63]. These evaluation metrics were selected based on[64]. Results for Dice, sensitivity, specificity and area under the receiver-operating characteristic curve (AUC) are shown in Fig. 8. Here, the gray boxplots are the accuracy measurements when ADC maps were thresholded between 800 and 1100 $\mu m^2/s$ (50 $\mu m^2/s$ intervals). The blue boxplots are the accuracy measurements when the Z_{ADC} maps were thresholded at -1.5, -2, and -2.5. Figure 8 demonstrates: (i) both ADC and Z_{ADC} have values in helping segment the HIE-related lesions, since the specificity from simple naive thresholding-based segmentations was comparable to those from machine learning-based algorithms[20], although the Dice and sensitivity were lower; (ii) Z_{ADC} maps thresholded at -2, the most intuitive and straightforward threshold value, yielded the highest Dice (0.54 ± 0.28), followed by Z_{ADC} maps thresholded at -2.5 (Dice 0.39 ± 0.25); (iii) Z_{ADC} maps thresholded at -1.5 yielded the highest $\frac{sensitivity^2 + specificity^2}{2}$ (0.82 ± 0.02), quantifying the balance between sensitivity and specificity compared with any ADC thresholds, followed by Z_{ADC} maps thresholded at -2 (0.76 ± 0.03); and (iv) overall, across all thresholds, Z_{ADC} maps showed a higher area under the curve (AUC: 0.936). Meanwhile, accuracies measured by MASD (lower MASD for a higher accuracy) and NSD (higher NSD for a higher accuracy), confirmed that Z_{ADC} map's superior accuracy than ADC maps. This shows that Z_{ADC} maps – anatomy-normalized ADC images – carry the potential to improve lesion detection accuracy compared to ADC maps.

Code availability

No custom code was generated for this work.

Received: 31 January 2024; Accepted: 2 September 2024;
Published online: 11 January 2025

References

1. Rutherford, M. *et al.* Magnetic resonance imaging in hypoxic-ischaemic encephalopathy. *Early Human Development* **86**, 351–360 (2010).
2. Shankaran, S. *et al.* Brain injury following trial of hypothermia for neonatal hypoxic–ischaemic encephalopathy. *Archives of Disease in Childhood-Fetal and Neonatal Edition* **97**, F398–F404 (2012).
3. Weeke, L. C. *et al.* A novel magnetic resonance imaging score predicts neurodevelopmental outcome after perinatal asphyxia and therapeutic hypothermia. *The Journal of Pediatrics* **192**, 33–40 (2018).
4. Graham, E. M., Ruis, K. A., Hartman, A. L., Northington, F. J. & Fox, H. E. A systematic review of the role of intrapartum hypoxia-ischemia in the causation of neonatal encephalopathy. *American Journal of Obstetrics and Gynecology* **199**, 587–595 (2008).
5. Lee, A. C. *et al.* Intrapartum-related neonatal encephalopathy incidence and impairment at regional and global levels for 2010 with trends from 1990. *Pediatric Research* **74**, 50–72 (2013).
6. Weiss, R. J. *et al.* Mining multi-site clinical data to develop machine learning mri biomarkers: application to neonatal hypoxic ischemic encephalopathy. *Journal of Translational Medicine* **17**, 1–16 (2019).
7. Herrera, T. I. *et al.* Outcomes of preterm infants treated with hypothermia for hypoxic-ischemic encephalopathy. *Early Human Development* **125**, 1–7 (2018).
8. Inder, T. E. *et al.* Randomized trial of systemic hypothermia selectively protects the cortex on mri in term hypoxic-ischemic encephalopathy. *The Journal of Pediatrics* **145**, 835–837 (2004).
9. Rogers, E. E. *et al.* Erythropoietin and hypothermia for hypoxic-ischemic encephalopathy. *Pediatric Neurology* **51**, 657–662 (2014).
10. Natarajan, G., Pappas, A. & Shankaran, S. Outcomes in childhood following therapeutic hypothermia for neonatal hypoxic-ischemic encephalopathy (HIE). In *Seminars in Perinatology*, vol. 40, 549–555 (Elsevier, 2016).
11. Ramaswamy, V. *et al.* Systematic review of biomarkers of brain injury in term neonatal encephalopathy. *Pediatric Neurology* **40**, 215–226 (2009).
12. van Laerhoven, H., de Haan, T. R., Offringa, M., Post, B. & van der Lee, J. H. Prognostic tests in term neonates with hypoxic-ischemic encephalopathy: a systematic review. *Pediatrics* **131**, 88–98 (2013).
13. Laptook, A. R. *et al.* Effect of therapeutic hypothermia initiated after 6 hours of age on death or disability among newborns with hypoxic-ischemic encephalopathy: a randomized clinical trial. *JAMA* **318**, 1550–1560 (2017).
14. Shankaran, S. *et al.* Effect of depth and duration of cooling on death or disability at age 18 months among neonates with hypoxic-ischemic encephalopathy: a randomized clinical trial. *JAMA* **318**, 57–67 (2017).
15. O'Mara, K. & Weiss, M. D. Dexmedetomidine for sedation of neonates with HIE undergoing therapeutic hypothermia: a single-center experience. *American Journal of Perinatology Reports* **8**, e168–e173 (2018).
16. Massaro, A. N. *et al.* Serum biomarkers of mri brain injury in neonatal hypoxic ischemic encephalopathy treated with whole-body hypothermia: a pilot study. *Pediatric Critical Care Medicine* **14**, 310–317 (2013).
17. Massaro, A. N. *et al.* Plasma biomarkers of brain injury in neonatal hypoxic-ischemic encephalopathy. *The Journal of Pediatrics* **194**, 67–75 (2018).
18. Douglas-Escobar, M. & Weiss, M. D. Biomarkers of hypoxic-ischemic encephalopathy in newborns. *Frontiers in Neurology* **3**, 144 (2012).
19. Ronneberger, O., Fischer, P. & Brox, T. U-net: Convolutional networks for biomedical image segmentation. In *International Conference on Medical Image Computing and Computer-Assisted Intervention*, 234–241 (Springer, 2015).
20. Murphy, K. *et al.* Automatic quantification of ischemic injury on diffusion-weighted mri of neonatal hypoxic ischemic encephalopathy. *NeuroImage: Clinical* **14**, 222–232 (2017).
21. Menze, B. H. *et al.* The multimodal brain tumor image segmentation benchmark (brats). *IEEE Transactions on Medical Imaging* **34**, 1993–2024 (2014).

22. Bakas, S. *et al*. Advancing the cancer genome atlas glioma mri collections with expert segmentation labels and radiomic features. *Scientific Data* **4**, 1–13 (2017).
23. Bakas, S. *et al*. Identifying the best machine learning algorithms for brain tumor segmentation, progression assessment, and overall survival prediction in the brats challenge. *arXiv preprint arXiv:1811.02629* (2018).
24. Maier, O. *et al*. Isles 2015-a public evaluation benchmark for ischemic stroke lesion segmentation from multispectral mri. *Medical Image Analysis* **35**, 250–269 (2017).
25. Carass, A. *et al*. Longitudinal multiple sclerosis lesion segmentation: resource and challenge. *NeuroImage* **148**, 77–102 (2017).
26. Commowick, O. *et al*. Objective evaluation of multiple sclerosis lesion segmentation using a data management and processing infrastructure. *Scientific Reports* **8**, 13650 (2018).
27. Antonelli, M. *et al*. The medical segmentation decathlon. *Nature Communications* **13**, 4128 (2022).
28. Isensee, F., Jaeger, P. F., Kohl, S. A., Petersen, J. & Maier-Hein, K. H. nnu-net: a self-configuring method for deep learning-based biomedical image segmentation. *Nature Methods* **18**, 203–211 (2021).
29. Murphy, S. N. *et al*. High throughput tools to access images from clinical archives for research. *Journal of Digital Imaging* **28**, 194–204 (2015).
30. Provenzale, J. M., Liang, L., DeLong, D. & White, L. E. Diffusion tensor imaging assessment of brain white matter maturation during the first postnatal year. *American Journal of Roentgenology* **189**, 476–486 (2007).
31. Dudink, J. *et al*. Fractional anisotropy in white matter tracts of very-low-birth-weight infants. *Pediatric Radiology* **37**, 1216–1223 (2007).
32. Forman, C., Wetzl, J., Hayes, C. & Schmidt, M. Compressed sensing: a paradigm shift in mri. *MAGNETOM Flash* **66**, 9–13 (2016).
33. Tustison, N. J. *et al*. N4ITK: improved n3 bias correction. *IEEE Transactions on Medical Imaging* **29**, 1310–1320 (2010).
34. Ou, Y. *et al*. Field of view normalization in multi-site brain mri. *Neuroinformatics* **16**, 431–444 (2018).
35. Ou, Y. *et al*. Brain extraction in pediatric adc maps, toward characterizing neuro-development in multi-platform and multi-institution clinical images. *NeuroImage* **122**, 246–261 (2015).
36. Ou, Y. *et al*. Using clinically acquired mri to construct age-specific adc atlases: Quantifying spatiotemporal adc changes from birth to 6-year old. *Human Brain Mapping* **38**, 3052–3068 (2017).
37. Ou, Y., Sotiras, A., Paragios, N. & Davatzikos, C. Dramms: Deformable registration via attribute matching and mutual-saliency weighting. *Medical Image Analysis* **15**, 622–639 (2011).
38. Ou, Y., Akbari, H., Bilello, M., Da, X. & Davatzikos, C. Comparative evaluation of registration algorithms in different brain databases with varying difficulty: results and insights. *IEEE Transactions on Medical Imaging* **33**, 2039–2065 (2014).
39. Pinto, A. L., Ou, Y., Sahin, M. & Grant, P. E. Quantitative apparent diffusion coefficient mapping may predict seizure onset in children with sturge-weber syndrome. *Pediatric Neurology* **84**, 32–38 (2018).
40. He, S. *et al*. Multi-channel attention-fusion neural network for brain age estimation: accuracy, generality, and interpretation with 16,705 healthy mris across lifespan. *Medical Image Analysis* **72**, 102091 (2021).
41. He, S., Grant, P. E. & Ou, Y. Global-local transformer for brain age estimation. *IEEE Transactions on Medical Imaging* **41**, 213–224 (2021).
42. He, S., Feng, Y., Grant, P. E. & Ou, Y. Deep relation learning for regression and its application to brain age estimation. *IEEE Transactions on Medical Imaging* **41**, 2304–2317 (2022).
43. Khoury, J. E. *et al*. Maternal childhood maltreatment is associated with lower infant gray matter volume and amygdala volume during the first two years of life. *Biological psychiatry global open science* **2**, 440–449 (2022).
44. Douglas-Escobar, M. & Weiss, M. D. Hypoxic-ischemic encephalopathy: a review for the clinician. *JAMA Pediatrics* **169**, 397–403 (2015).
45. Wei, R. *et al*. Prediction of poor outcome after hypoxic-ischemic brain injury by diffusion-weighted imaging: A systematic review and meta-analysis. *Plos One* **14**, e0226295 (2019).
46. Liauw, L., van Wezel-Meijler, G., Veen, S., Van Buchem, M. & van der Grond, J. Do apparent diffusion coefficient measurements predict outcome in children with neonatal hypoxic-ischemic encephalopathy? *American Journal of Neuroradiology* **30**, 264–270 (2009).
47. Sotardi, S. *et al*. Voxelwise and regional brain apparent diffusion coefficient changes on mri from birth to 6 years of age. *Radiology* **298**, 415 (2021).
48. Liu, L., Wolterink, J. M., Brune, C. & Veldhuis, R. N. Anatomy-aided deep learning for medical image segmentation: a review. *Physics in Medicine & Biology* **66**, 11TR01 (2021).
49. Bao, R., Ou, Y. & Grant, E. BOston Neonatal Brain Injury Data for Hypoxic Ischemic Encephalopathy (BONBID-HIE): I. MRI and Manual Lesion Annotation Version V3. *Zenodo*, https://zenodo.org/records/10602767 (2024).
50. Imanishi, T. *et al*. Brain injury following mild hypoxic-ischemic encephalopathy in neonates–ten-year experience in a tertiary perinatal center. *Journal of Perinatology* 1–7 (2022).
51. Li, Y. *et al*. Mild hypoxic-ischemic encephalopathy (HIE): Timing and pattern of mri brain injury. *Pediatric Research* 1–6 (2022).
52. Chalak, L., Latremouille, S., Mir, I., Sánchez, P. J. & Sant'Anna, G. A review of the conundrum of mild hypoxic-ischemic encephalopathy: Current challenges and moving forward. *Early Human Development* **120**, 88–94 (2018).
53. Barkovich, A. J. *et al*. Prediction of neuromotor outcome in perinatal asphyxia: evaluation of mr scoring systems. *American Journal of Neuroradiology* **19**, 143–149 (1998).
54. Trivedi, S. B. *et al*. A validated clinical mri injury scoring system in neonatal hypoxic-ischemic encephalopathy. *Pediatric Radiology* **47**, 1491–1499 (2017).
55. Hunt, R. W., Neil, J. J., Coleman, L. T., Kean, M. J. & Inder, T. E. Apparent diffusion coefficient in the posterior limb of the internal capsule predicts outcome after perinatal asphyxia. *Pediatrics* **114**, 999–1003 (2004).
56. van der Aa, N. E., Benders, M. J., Vincken, K. L., Groenendaal, F. & de Vries, L. S. The course of apparent diffusion coefficient values following perinatal arterial ischemic stroke. *PLoS One* **8**, e56784 (2013).
57. He, S., Feng, Y., Grant, P. E. & Ou, Y. Segmentation ability map: Interpret deep features for medical image segmentation. *Medical Image Analysis* **84**, 102726 (2023).
58. Kushwah, S., Kumar, A., Verma, A., Basu, S. & Kumar, A. Comparison of fractional anisotropy and apparent diffusion coefficient among hypoxic ischemic encephalopathy stages 1, 2, and 3 and with nonasphyxiated newborns in 18 areas of brain. *Indian Journal of Radiology and Imaging* **27**, 447–456 (2017).
59. Shibasaki, J. *et al*. Comparison of predictive values of magnetic resonance biomarkers based on scan timing in neonatal encephalopathy following therapeutic hypothermia. *The Journal of Pediatrics* **239**, 101–109 (2021).
60. Al Amrani, F. *et al*. Early imaging and adverse neurodevelopmental outcome in asphyxiated newborns treated with hypothermia. *Pediatric Neurology* **73**, 20–27 (2017).
61. Heursen, E.-M. *et al*. Prognostic value of the apparent diffusion coefficient in newborns with hypoxic-ischaemic encephalopathy treated with therapeutic hypothermia. *Neonatology* **112**, 67–72 (2017).
62. Beneš, M. & Zitová, B. Performance evaluation of image segmentation algorithms on microscopic image data. *Journal of Microscopy* **257**, 65–85 (2015).
63. Reinke, A. *et al*. Common limitations of image processing metrics: A picture story. *arXiv preprint arXiv:2104.05642* (2021).
64. Maier-Hein, L. et al. Metrics reloaded: recommendations for image analysis validation. *Nature Methods* 1–18 (2024).

Acknowledgements
This work was funded, in part, by the Harvard Medical School and Boston Children's Hospital through Early Career Development Fellowship, Thrasher Research Fund Early Career Awards, NIH R21NS121735, R61NS126792, and R03HD104891.

Author contributions
Study Design: R.B., S.V.B., A.N.F., R.L.H., P.E.G., Y.O.; Data Collection: S.V.B., R.J.W., A.N.F., R.L.H., P.E.G., Y.O.; Data Analysis: R.B., Y.S., S.B.V., R.J.W., A.N.F., C.J.C., S.S., Y.Z., R.L.H., P.E.G., Y.O.; Manuscript Writing: R.B., S.V.B., A.N.F., R.L.H., P.E.G., Y.O.

Competing interests
The authors declare no competing interests.

Additional information
Correspondence and requests for materials should be addressed to R.B. or Y.O.

Reprints and permissions information is available at www.nature.com/reprints.

Publisher's note Springer Nature remains neutral with regard to jurisdictional claims in published maps and institutional affiliations.